Journal of Manufacturing Processes 84 (2022) 260–271

Contents lists available at ScienceDirect

Journal of Manufacturing Processes

journal homepage: www.elsevier.com/locate/manpro

On the effect of scan strategies on the transformation behavior and mechanical properties of additively manufactured NiTi shape memory alloys

Chen Zhang [a], Hande Ozcan [b], Lei Xue [b], Kadri C. Atli [b], Raymundo Arróyave [b], Ibrahim Karaman [b], Alaa Elwany [a,*]

[a] Wm Michael Barnes '64 Department of Industrial and Systems Engineering, Texas A&M University, College Station, TX, United States
[b] Department of Materials Science and Engineering, Texas A&M University, College Station, TX, United States

ARTICLE INFO

Keywords:
Laser powder bed fusion (L-PBF)
Additive manufacturing (AM)
Shape memory alloy (SMA)
NiTi
Scan strategy
Phase transformation
Warping deformation

ABSTRACT

Laser-powder bed fusion (L-PBF) additive manufacturing (AM) presents excellent potential to fabricate geometrically complex structures with tailored microstructures and compositions from nickel titanium shape memory alloys (NiTi SMAs). The effect of common L-PBF process parameters, such as laser power, scanning speed, and hatch spacing, have been reported in many literature studies. However, one important factor that has not been investigated is the laser scan strategy, or the path that the laser follows within each layer. This is a particularly important factor to investigate in the case of NiTi SMAs that tend to be more sensitive to thermal histories than other commercial AM materials. For example, even slight variations in thermal history might exhibit notable influence on transformation behavior due to composition changes resulting from differential evaporation of nickel. The current work presents a first investigation on such effects of 12 laser scan strategy on the fabrication outcome of additively manufactured Ni-rich NiTi SMAs. The extent of warping deformation and surface morphology of fabricated parts with different scan strategies were found to show notable differences. Some phase transformation variations among different scan strategies were also identified in as-fabricated and solution heat treated conditions, although these variations were not as pronounced as variations in warping due to residual stresses and surface morphology. This study guides the selection of scan strategies such that build failures due to excessive warping and poor surface morphology are minimized. It also provides additional flexibility in controlling mechanical properties and phase transformation behavior of this relatively difficult-to-process class of materials.

1. Introduction

Nickle-titanium (NiTi) shape memory alloys (SMAs) were discovered in 1959 by William J. Buehler and Frederick Wang [1,2]. This class of alloys has some unique properties, such as the ability to retain their original shapes after deformation upon being heated due to reversible temperature-induced phase transformation between austenite and martensite [3]. On account of other favorable characteristics, such as superelasticity, biocompatibility, and corrosion resistance, NiTi SMAs have found a wide range of applications in biomedical, aerospace and thermal applications [4–7]. Due to the challenges associated with using traditional manufacturing and processing routes (e.g. casting, forging, or machining), additive manufacturing (AM) technologies have recently been identified as attractive alternatives [8]. In particular, laser-powder bed fusion (L-PBF) process has been most commonly used to fabricate NiTi SMA parts due to its high printing resolution, ability to keep the oxygen content at very low levels, and excellent printing quality [9].

In order to manufacture NiTi SMA parts with desired mechanical properties and phase transformation behavior, in-depth understanding of the relationship between manufacturing process conditions and part properties is critical. Previous works primarily focused on investigating the effects of key process parameters (e.g. laser power (P), laser scanning speed (v)) [10–13] or some combination of those parameters (linear or volumetric energy density defined as E_L [14] and E_V [15] in Eqs. (1) and (2), respectively, where t is the powder layer thickness and h is the hatch spacing) [16–20] on the properties of L-PBF fabricated NiTi. For

* Corresponding author.
E-mail address: elwany@tamu.edu (A. Elwany).

https://doi.org/10.1016/j.jmapro.2022.09.051
Received 25 April 2022; Received in revised form 28 August 2022; Accepted 23 September 2022
Available online 14 October 2022

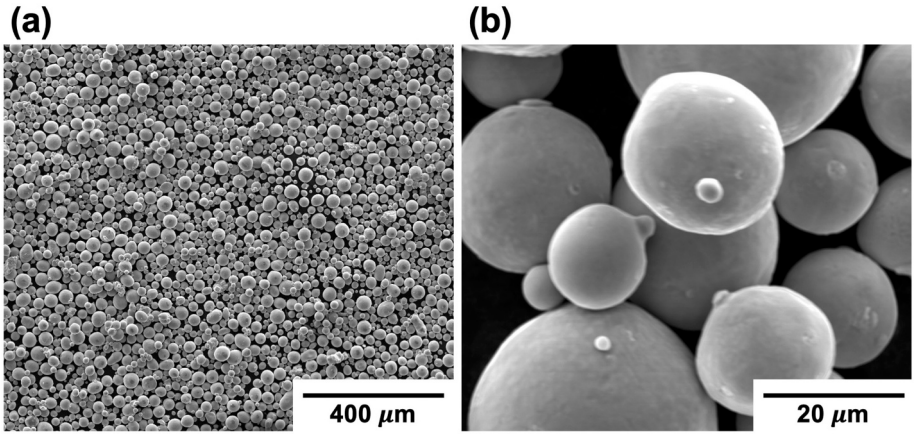

Fig. 1. Morphology of $Ni_{50.8}Ti_{49.2}$ (at.%) powder utilized in the current study obtained using scanning electron microscopy (SEM) in (a) low and (b) high magnifications.

example, Mahmoudi et al. [9] investigated the effects of both E_L and E_V on the manufacturability and phase transformation behavior of Ni-rich NiTi and concluded that E_L played a more significant role than E_V in predicting manufacturability (or printability) while E_V had correlation with the martensitic transformation temperatures. Some studies in the literature report similar observations [16,17,21]. Other studies highlighted the importance of studying the effects of individual parameters, in contrast to aggregate metrics like E_L and E_V [18,19,22].

$$E_L = \frac{P}{v} \tag{1}$$

$$E_v = \frac{P}{h \cdot v \cdot t} \tag{2}$$

Despite the wealth of literature studies on the effects of P, v, h, E_L, and E_V on the properties of L-PBF processed NiTi materials, there is another important factor that has received relatively limited attention: the laser scan strategy. The laser scan strategy refers to the scanning path of the laser beam within and between successive layers when printing parts with L-PBF, which plays an important role in controlling the transient thermal history of the manufacturing process. This in turn subsequently has an impact on the microstructure, final material composition, texture orientation and residual stress accumulation, all of which affect the quality and mechanical and functional properties of the final part. That is, even if other laser process parameters such as P, v, h, and t remain constant, a simple modification of the laser scan strategy may result in a significant change in part performance. Therefore, it is of high importance to investigate the effect of laser scan strategy on L-PBF fabricated NiTi parts in order to improve the printing quality and thus optimize the mechanical and functional properties, as well as to eventually expand the application prospects of L-PBF processed NiTi materials.

There are several studies in the literature that highlight the effects of the laser scan strategy in other material systems (e.g., steels, aluminum alloys, Ni-based superalloys, etc.). The focus of these literature studies is mainly on investigating the impact of the scan strategy on density/porosity, microstructure, texture, residual stresses, and mechanical properties of fabricated parts through numerical simulations or experimental methods. On the experimental side, Gouveia et al. [23] investigated the effect of four different laser scan strategies on the density, residual stress, surface roughness and hardness of AlSi10Mg parts and concluded that no single scan strategy outperformed the others in all performance metrics. In another study, Rashid et al. [24] investigated the effect of three different laser scan strategies on the final part density and showed that the hexagonal scan strategy resulted in the highest relative density of the printed AlSi12 alloys. Zhang et al. [25] also compared the final part densities produced by three different scan strategies in printed 17–4 stainless steel and recommended that the scan strategy with the lowest energy consumption was to be selected provided that target properties are met. Arisoy et al. [26] evaluated the effect of scan strategy on grain size, grain growth and orientation of printed Inconel 625 nickel superalloys and concluded that a stripe scan strategy with a rotation angle of 67 °C produced finer grains. The hexagonal scan strategy was shown to result in the highest ultimate tensile strength of the printed 17–4 stainless steel in the study conducted by Kudzal et al. [27]. In terms of numerical simulations, Ramos et al. [28] applied a coupled thermomechanical computational model to investigate the effects of five different laser scan strategies on the transient temperature field, residual stress field and deformation during the fabrication of Ti-6Al-4 V material and concluded that shorter scan vector lengths resulted in lower residual stresses and a smaller degree of deformation. Song et al. [29] studied three scan strategies through finite element analysis and found out that a rotation angle of 15 °C produced the lowest residual stress in the fabrication of Ti-6Al-4 V alloys. The simulation performed on In718 alloys investigated eight different scan strategies and the results showed that the 45 °C line scan strategy exhibited both a smaller residual stress and less deformation compared to the in-out scanning case, as reported by Cheng et al. [30]. It is worth mentioning that due to high computational cost of finite element simulations, most of the numerical simulation work was performed on a single layer or several layers rather than on the whole part. This would have an impact on the real reliability of the simulation results.

Although a handful of literature studies investigated the effects of some common laser scan strategies and devised new scan strategies for potential implementation in commercial L-PBF systems, this area of research is still at early stages relative to other well-studied L-PBF process parameters. In the particular case of NiTi SMAs, the effects of scan strategy on the printability, transformation behavior, and mechanical properties is entirely lacking. Such investigation is especially important due to the extreme sensitivity of NiTi to residual stresses and potential process-induced defects that are common to L-PBF processes. This study aims to fill this literature gap through systematically investigating the effects of 12 different laser scan strategies on the density, residual stress, phase transformation behavior, and mechanical properties of Ni-rich NiTi SMAs fabricated using L-PBF AM. The rest of the paper is organized as follows: Section 2 provides details of the experimental methods and test bed employed in the study. Discussion of experimental results is presented in Section 3. Section 4 draws concluding remarks and lays out directions for future research.

Table 1
Constant laser process parameters utilized for cubic samples fabrication. Apart from the scan strategy, all other process parameters are kept constant for all samples.

Laser power (W)	Scan speed (mm/s)	Hatch spacing (μm)	Layer thickness (μm)	E_L (J/m)	E_V (J/mm^3)
200	1080	80	38	185.19	60.92

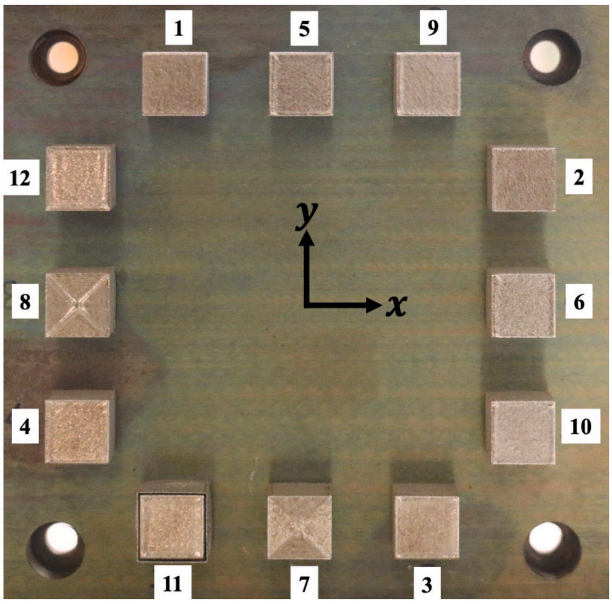

Fig. 2. As-printed NiTi samples fabricated by L-PBF process. The numeric labels from 1 to 12 indicate the order in which samples were scanned within each layer.

2. Materials and experimental methods

2.1. Powder characterization

The slightly Ni-rich NiTi powder utilized in this study was provided by Carpenter Technology Corp prepared by the electrode induction-melting gas atomization (EIGA) method. Differential scanning calorimetry (DSC) characterization was conducted on both as-received and solution heat treated (950 °C for 24 h + water quenching) powder to measure the transformation temperatures and estimate the chemical composition. The powder was tested and shown to have a composition of $Ni_{50.8}Ti_{49.2}$ (at.%) [31]. Fig. 1 shows the morphology of the as-received powder captured by scanning electron microscopy (SEM, FEI Quanta 600 FE). The majority of the powder particles exhibit spherical and smooth morphology with particle diameters ranging between 10 and 60 μm, while very few satellite particles are observed. The D50 and D80 of the powder were 29 μm and 38 μm respectively, indicating that 50 % of the powder particles possessed a diameter <29 μm and 80 % of the powder particles possessed a diameter <38 μm respectively.

2.2. Sample fabrication

Twelve 10 × 10 × 10 mm^3 cubic samples were printed on a NiTi substrate using different laser scan strategies. Fabrication was done on a 3D Systems ProX 200 commercial L-PBF system employing a continuous Ytterbium fiber laser with wavelength 1070 nm, beam diameter 80 μm, and 300 W maximum power. All other laser process parameters than scan strategy were kept constant for all the samples, as listed in Table 1. These parameters were set at their optimized values determined by the co-authors in a previous study [31] that result in minimum porosity. Fabrication was conducted under an argon atmosphere, with oxygen level inside the build chamber maintained below 500 ppm. The cubes were arranged such that the thermal distribution on the build plate is as uniform as possible, as shown in Fig. 2, in which the numeric labels from 1 to 12 indicate the sequence to scan these samples.

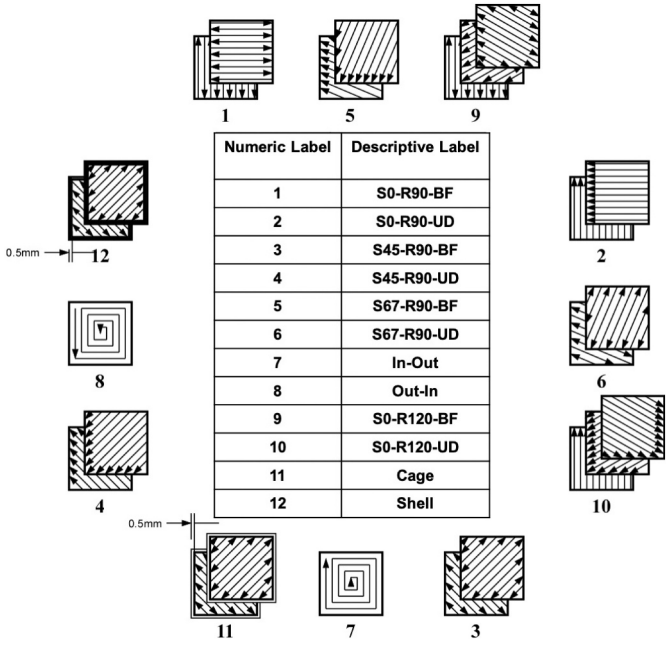

Numeric Label	Descriptive Label
1	S0-R90-BF
2	S0-R90-UD
3	S45-R90-BF
4	S45-R90-UD
5	S67-R90-BF
6	S67-R90-UD
7	In-Out
8	Out-In
9	S0-R120-BF
10	S0-R120-UD
11	Cage
12	Shell

Fig. 3. Schematic diagram of the twelve scan strategies investigated in this study. The samples were scanned by the laser in a sequence according to the numeric labels to homogenize the temperature field across the build plate.

The twelve different scan strategies utilized in this study are schematically illustrated in Fig. 3. Similar to Fig. 2, the numeric labels from 1 to 12 indicate the sequence of scanning the samples. Corresponding descriptive labels are also shown in Fig. 3, which are utilized to refer to the scan strategies in the remainder of the paper. Detailed description of each scan strategy is as follows:

1. Starting angle 0 °C, rotation angle 90 °C, back and forth scan strategy ("S0-R90-BF"). The laser scans the powder layer in a back and forth pattern while scanning the first layer along the *x*-axis direction and scan angle rotates 90 °C from layer to layer.
2. Starting angle 0 °C, rotation angle 90 °C, uni-directional scan strategy ("S0-R90-UD"). The laser scans the powder layer in a uni-directional pattern while scanning the first layer along the *x*-axis direction and scan angle rotates 90 °C from layer to layer.
3. Starting angle 45 °C, rotation angle 90 °C, back and forth scan strategy ("S45-R90-BF"). The laser scans the powder layer in a back and forth pattern while scanning the first layer at an angle of 45 °C to the *x*-axis direction and scan angle rotates 90 °C from layer to layer.
4. Starting angle 45 °C, rotation angle 90 °C, uni-directional scan strategy ("S45-R90-UD"). The laser scans the powder layer in a uni-directional pattern while scanning the first layer at an angle of 45 °C to the *x*-axis direction and scan angle rotates 90 °C from layer to layer.
5. Starting angle 67 °C, rotation angle 90 °C, back and forth scan strategy ("S67-R90-BF"). The laser scans the powder layer in a back and forth pattern while scanning the first layer at an angle of 67 °C to the *x*-axis direction and scan angle rotates 90 °C from layer to layer.
6. Starting angle 67 °C, rotation angle 90 °C, uni-directional scan strategy ("S67-R90-UD"). The laser scans the powder layer in a

Table 2
Total laser travel time, laser sintering time, and laser jumping time of each 10 × 10 × 10 mm^3 cubic sample fabricated by different laser scan strategies.

Numeric label	Laser scan strategy	Laser travel time (s)	Laser sintering time (s)	Laser jumping time (s)
1	S0-R90-BF	326	312	14
2	S0-R90-UD	388	312	76
3	S45-R90-BF	335	312	23
4	S45-R90-UD	400	312	88
5	S67-R90-BF	334	312	22
6	S67-R90-UD	396	312	84
7	In-Out	320	312	8
8	Out-In	320	312	8
9	S0-R120-BF	331	312	19
10	S0-R120-UD	394	312	82
11	Cage	349	312	37
12	Shell	346	312	34

uni-directional pattern while scanning the first layer at an angle of 67 °C to the *x*-axis direction and scan angle rotates 90 °C from layer to layer.

7. Concentric in-out scan strategy ("In-Out"). The laser scans the powder layer continuously from the center toward the periphery of the designed geometry.
8. Concentric out-in scan strategy ("Out-In"). The laser scans the powder layer continuously from the periphery toward the center of the designed geometry.
9. Starting angle 0 °C, rotation angle 120 °C, back and forth scan strategy ("S0-R120-BF"). The laser scans the powder layer in a back and forth pattern while scanning the first layer along the *x*-axis direction. The laser scanning direction rotates 120 °C layer by layer.
10. Starting angle 0 °C, rotation angle 120 °C, uni-directional scan strategy ("S0-R120-UD"). The laser scans the powder layer in a uni-directional pattern while scanning the first layer along the *x*-axis direction. The laser scanning direction rotates 120 °C layer by layer.
11. Cage scan strategy ("Cage"). The laser scans an outline outside the designed geometry first. The distance between the outline and the periphery of the designed geometry was set as 0.5 mm. After the outline being printed, the laser scans the designed geometry using "S45-R90-BF" scan strategy.
12. Shell scan strategy ("Shell"). The laser scans a 0.5 mm shell of the designed geometry using the "Out-In" scan strategy first. After the shell being printed, the laser scans the powder layer using "S45-R90-BF" scan strategy for the remaining core section of the designed geometry.

It is worth mentioning that scan strategies which separated the printing area into multiple small subsections (hexagon, island, and stripe scan strategies) were not considered in the current study, mainly due to the extra consideration requirements on the size, shape, overlap, and printing sequence of each small subsection, which also have significant effects on the L-PBF fabricated samples according to previous studies [32,33], and would possibly conceal the pattern to be investigated in the current study.

During L-PBF process, once a layer of powder has been evenly spread, the laser begins to scan, melt, and solidify the powder layer according to the geometry of the sliced CAD model. Based on the scan strategy, after the laser has finished sintering the current track, it turns off and jumps to the start of the next point to start the next weld track until the full layer is printed. In other words, the total time is the sum of the powder spreading time and the laser travel time, where the laser travel time can be further divided into the laser sintering time and the laser jumping time. While different scan strategies share the same powder spreading time and laser sintering time to fabricate samples with the same geometry and orientation at the same laser scanning speed and hatch spacing, the total time will be different due to differences in jumping times among scanning strategies. The total laser travel time, laser sintering time, and the laser jumping time for the 10 mm × 10 mm × 10 mm cubic sample with 12 different scan strategies are listed in Table 2. It can be seen that there is a difference of 80 s between the fastest (In-Out and Out—In) and slowest (S45-R90-UD) scan strategies. Although such difference is not significant when fabricating small parts, it will be exacerbated in the case of larger scale parts. In addition, the difference in laser jumping time also has an effect on the transient thermal histories, which in turn affect the phase transformation behavior of fabricated NiTi parts, as will be detailed in the following sections.

2.3. Surface morphology characterization

SEM was employed to investigate the top surface morphology of the edge / corner area and the central area in as-fabricated cubic samples with different scan strategies. The study of the morphology of the central region of the top surface can help investigate the effect of the laser scan strategy on surface roughness. In addition, the importance of assessing the impact of the laser scan strategy on material accumulation in the corner region stems from the fact that the degree of material accumulation in that corner region directly affects both the printing process but also the quality of the as-printed part. Intuitively, the material accumulation around the corners can lead to swelling/elevation of the corners, which can in turn have negative influence on the geometrical accuracy of the fabricated part. It has also been reported in [34] that the elevated corner induced by material accumulation would be orders of magnitude higher than the powder layer thickness. During the L-PBF process, the elevated corner would protrude from the powder bed and

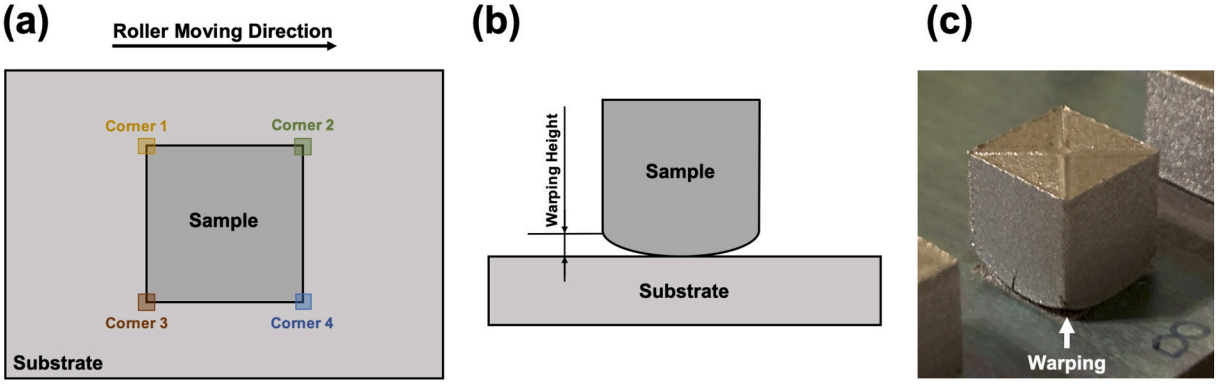

Fig. 4. Schematic diagram of (a) labels of each bottom corner of the fabricated cubic sample and (b) the warping height of one corner. (c) Photograph showing the warping phenomenon of a cubic sample fabricated using the laser scan strategy Out—In.

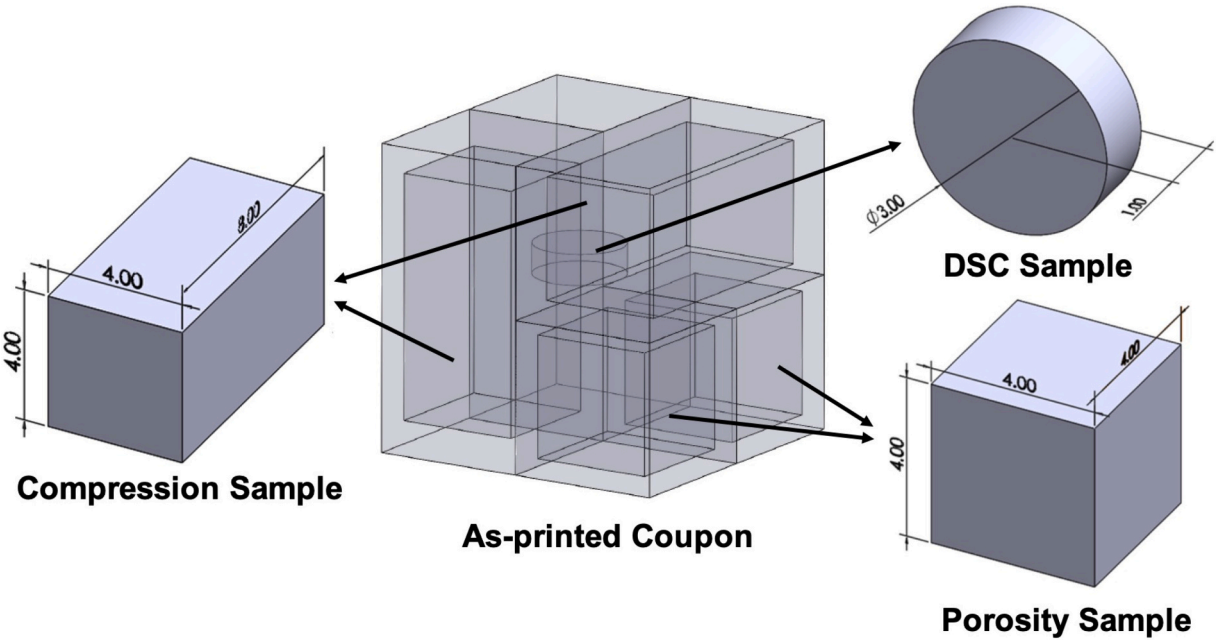

Fig. 5. Cutting scheme of as-printed cubic samples for DSC, porosity measurements, and compression mechanical testing. For each as-printed cubic sample, two 4 × 4 × 8 mm^3 rectangular prism compression samples, two 4 × 4 × 4 mm^3 cubic porosity samples, and one cylindrical DSC sample with 3 mm diameter and 1 mm thickness were EDM cut.

collide with the powder spreading mechanism such as the powder recoating roller or blade spreads the powder for the next layer, and would potentially cause early failure of the printing process. As reported in [35], the elevated corner is a common phenomenon in the fabrication of NiTi alloys with high Ni-content using L-PBF, and often occurs early in the fabrication process, with specimens with such defect often failing at very early stages. Therefore, mitigating the material accumulation around the corners by selecting the appropriate laser scan strategies is critical to improving the geometrical accuracy and the reliability of the fabrication process.

2.4. Warping deformation measurement

Warping is a common phenomenon in L-PBF, especially in the case of NiTi with high nickel content [36]. In earlier studies by the co-authors, warping was observed in samples fabricated using Ni-rich NiTi powder ($Ni_{51.2}Ti_{48.8}$), while for the near equiatomic counterpart ($Ni_{50.1}Ti_{49.9}$), the fabricated coupons were free of such defect [31,37]. A photograph of the warping phenomenon in a cubic sample fabricated by L-PBF using the laser scan strategy Out-In is shown in Fig. 4 (c). Warping is caused by the relief of residual stresses generated during the fabrication process due to transient thermal gradients, phase transformations, and chemical composition variations (Ni evaporation). When warping is severe, the printed samples can get detached from the substrate and cause failure of the entire fabrication process. Therefore, process parameters should be tailored and the effect of laser scan strategy on the warping behavior should be investigated to mitigate or avoid the warping deformation during the fabrication of Ni-rich NiTi SMAs. Warping was assessed by the warping height of four bottom corners, as illustrated in Fig. 4 (b), while the label for each corner is shown in Fig. 4 (a). The warping height of each bottom corner was measured by a digital vernier caliper before the samples were removed from the substrate.

2.5. Density and porosity measurements

Upon completion of the surface morphology characterization and warping deformation measurements, the fabricated parts were removed from the substrate by wire electrical discharge machining (EDM). The density of the fabricated samples was subsequently measured using Archimedes' method according to ASTM B962-17 standard. The as-fabricated parts were then cut into smaller samples for further characterization of microstructure, transformation behavior, and mechanical properties via EDM, as shown in Fig. 5. In order to quantify the porosity of the printed parts, the porosity samples were mounted and the cross-sections parallel to the building direction were ground with 1200 grit SiC paper. Cross-sectional images were captured by optical microscopy (OM, Keyence VHX-1000) and analyzed using image analysis software ImageJ to measure the areal percent porosity.

2.6. Transformation behavior analysis

The transformation behavior of fabricated samples in both as-printed and solution heat treated condition (800 °C for 1 h followed by water quenching) was characterized using a TA Instruments Q2000 DSC instrument on cylindrical DSC samples with 3 mm diameter and 1 mm thickness. Two DSC cycles from −150 °C to +150 °C with heating / cooling rate of 10 °C /min were applied. Transformation temperatures (martensite finish, M_f; martensite start, M_s; austenite start, A_s; austenite finish A_f) were determined using the method of tangent line intercept in the second cycle following ASTM F2004–17 in order to eliminate the first cycle effects. Thermal hysteresis was calculated thereafter.

2.7. Thermo-mechanical characterization

Thermomechanical characterization, including the incremental load tests and shape recovery tests, was performed on a servo-hydraulic MTS compression testing system with temperature control capability in the strain control mode with a strain rate of 5×10^{-4} s^{-1}. These tests were conducted on rectangular prism compression samples that were EDM cut from as-printed cubic samples, as shown in Fig. 5. The compression samples had a dimension of 4 × 4 × 8 mm^3, with the long edge parallel to the compressive loading direction.

Incremental load tests were conducted in order to characterize the superelasticity of fabricated samples. The compression sample was loaded with a compression strain starting from 1 % all the way to 8 % with 1 % increment each time and unloaded. The whole testing process

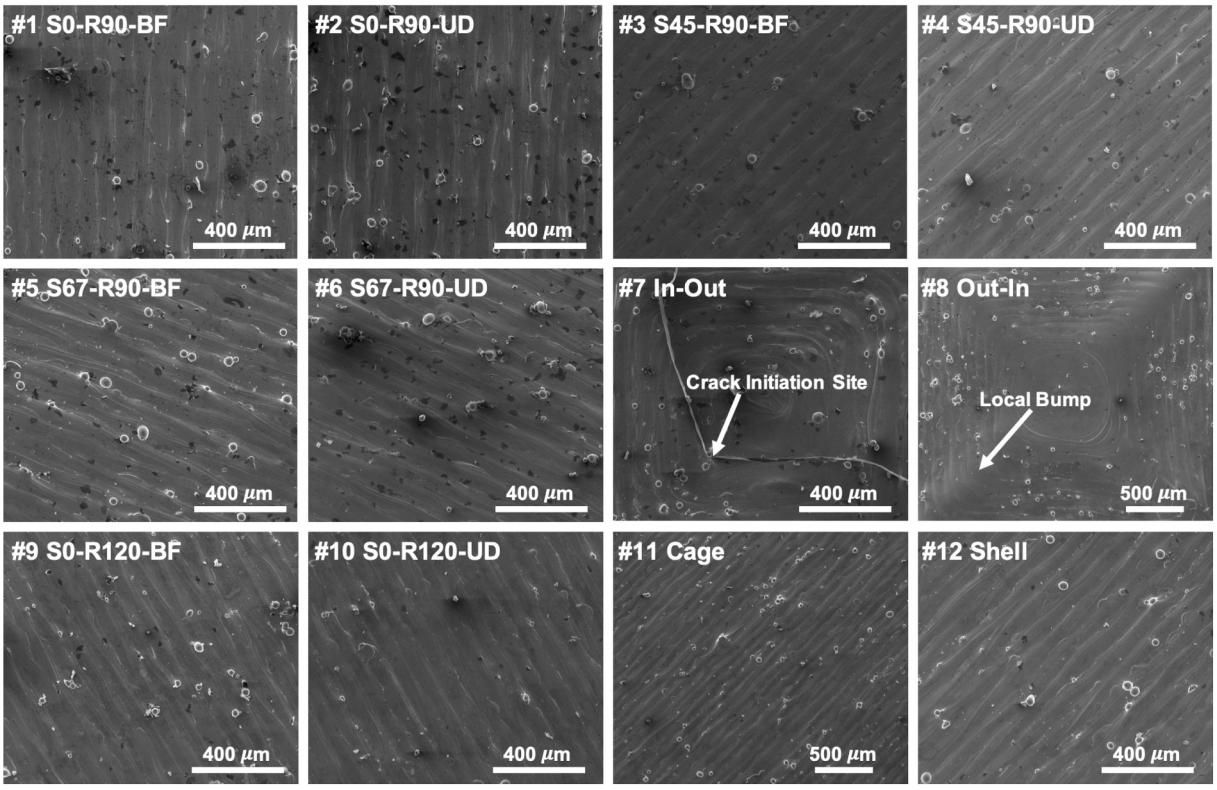

Fig. 6. SEM images of the central region of top surfaces fabricated with different laser scan strategies.

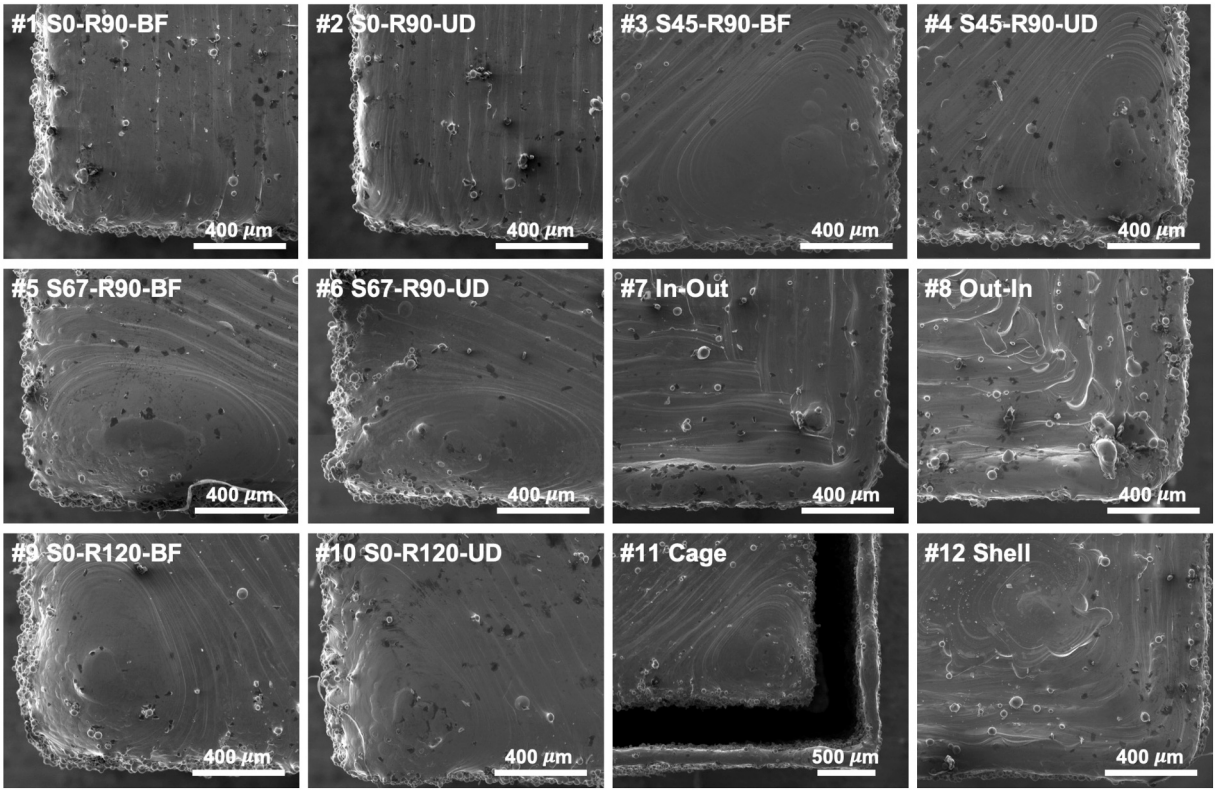

Fig. 7. SEM images of the corner region of top surfaces fabricated with different laser scan strategies.

was conducted at the temperature slightly above the A_f of each as-printed sample. The recoverable and irrecoverable strains were recorded for each loading-unloading cycle.

Shape recovery tests were conducted in order to characterize the shape memory effect of fabricated samples. The compression samples were compressed at −50 °C (in martensite) by increment of 2 % strain and unloaded, followed by heating up to 100 °C (in austenite) to measure the recovered and unrecovered deformations.

3. Characterization results and discussion

3.1. Surface morphology

The top surface morphologies of cubic samples fabricated using different laser scan strategies are shown in Fig. 6 and Fig. 7, in which middle and corner regions are captured respectively. As shown in Fig. 6, uniform and smooth surfaces were obtained by using uni-directional or back and forth scan strategies in the middle region (Samples #1 - #6, Samples #9 - #12), with spatter occasionally observed. The laser power and scanning speed used in this study were proved to result in uniform and smooth single tracks in our previous study [31]. In the middle region, the laser tracks generated by uni-directional or back and forth scan strategies reached a steady state, compared to the beginning and end of laser tracks. Therefore, a smooth surface morphology in the middle region was secured. On the contrary, for concentric Out-In scan strategy (Sample #8), local bumps were observed along the diagonal direction, which were caused by the instability of the melt pool near the diagonal. When the laser reaches the diagonal line of the square cross section, the change of laser scan direction resulted in an abrupt scanning speed decrease from setting value toward 0 along the previous scan direction, which subsequently increased the input energy and finally resulted in a significantly larger melt pool size in a short period of time. To avoid such melt pool instability, modifications in part geometry (e.g., introduce rounded corners) is recommended in order to prevent sharp turn of the laser scan direction. It is worth mentioning that in addition to degrading the surface integrity, the abrupt change of laser scan direction near the diagonal also lead to local residual stress concentration [30], and generates crack initiation sites. As shown in Fig. 6, cracks initiated on the diagonal are observed in Sample #7.

On the corner region, as shown in Fig. 7, the samples printed using different scan strategies exhibit notable difference. Among uni-directional and back and forth scan strategies (Samples #1 - #6, and Samples #9 - #10), S0-R90-BF and S0-R90-UD exhibit the most smooth corner region without noticeable material accumulation. Material accumulation is noticed in S45-R90-BF, while the uni-directional scan strategy marginally mitigated such material accumulation to a certain extent compared to back and forth scan strategy (compare Samples #3 and #4). Similar difference between uni-directional and back and forth scan strategies existed in other scan strategies (compare Samples #5 and #6, #9 and #10). For the back and forth scan strategy, laser starts to melt the powder material adjacent to the former generated melt track which does not have enough time for cooling, therefore the thermal gradient is smaller and the maximum attainable temperature is higher compared to the uni-directional counterpart, giving rise to a more significant material accumulation due to the enlargement of melt pool and entrapment of surrounding powder particles at a relatively high temperature (higher than melting temperature and sustains for a longer period of time). The shell scan strategy (Sample #12) mitigated such material accumulation at the corner by generating an outer shell prior to the melting of the inner area, which functions both as a heat sink that facilitates thermal dissipation and as an isolating wall separating the inner region and the outer powder material, and in turn reduced the material accumulation around the corner at the inner area. Due to the existence of the large gap between the cage (outline) and the core regions in the cage scan strategy (Sample #11), the cage didn't make a comparable difference to the shell in Sample #12. As a result, material accumulation still existed around the corner of the core region, which was scanned by the same scan strategy as Sample #3. No significant material accumulation existed in concentric scan strategies (Samples #7 and #8).

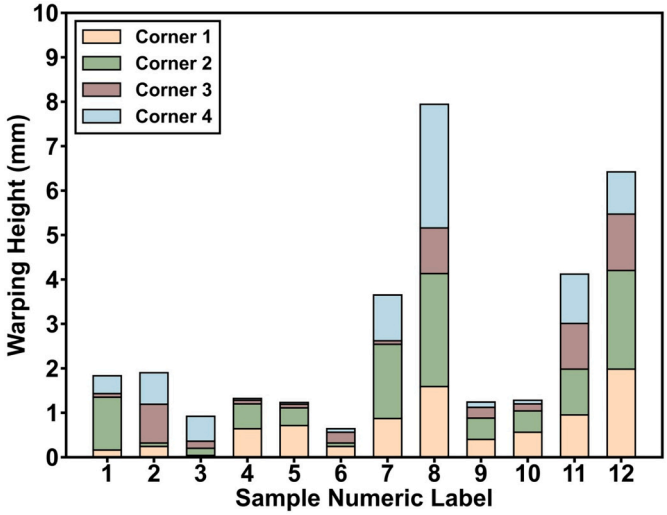

Fig. 8. Warping deformation magnitudes of L-PBF fabricated NiTi cubic samples using different laser scan strategies.

3.2. Warping due to residual stresses

Fig. 8 shows warping deformation magnitudes for the fabricated samples, indicating notable difference among different scan strategies. The concentric Out-In strategy (Sample #8) showed maximum warping deformation, while the normal S67-R90-UD strategy (Sample #6) showed minimum warping deformation. Concentric scan strategies are observed to generally result in larger warping deformation than uni-directional or back and forth scan strategies. One possible explanation is the fact that, on average, concentric scan strategies have longer laser scan vectors. It has been frequently reported that thermal stress generated along the laser path is a key contributor to residual stress build-up during L-PBF process due to high thermal gradient along the scanning vector direction [38]. With the increase of scanning vector length, residual stress increases, resulting in a higher magnitude of warping deformation [39,40]. Owing to the average laser scan vector length difference, the warping deformation associated with uni-directional or back and forth scan strategies was systematically less than concentric strategies. The result is consistent with what has been reported in [30], that concentric Out-In scan strategy provided the highest residual stresses. In addition, for uni-directional or back and forth scan strategies applied in this study, the scan vector rotation between consecutive layers avoided residual stress accumulation along a specific direction to a certain extent, while for the concentric scan strategies, scan vector direction was kept identical throughout the printing process, which is another possibility for the difference of warping deformation magnitude between uni-directional or back and forth scan strategies and concentric scan strategies.

It is worth mentioning that for Samples #11 and #12, the middle region of which were printed using back and forth scan strategies, significant warping deformation was still noticed. Such phenomenon could be explained by residual stress distribution in as-printed parts. According to [41], the maximum residual stress was observed close to the edges of printed samples, while the central area possessed a uniform stress distribution. As a result, scan strategy applied near the edge has a more significant impact on the residual stress build-up and resulting warping deformation compared to the scan strategy implemented in the central area. Therefore, for Samples #11 and #12, due to concentric scan

Table 3
The measured relative density and areal percent porosity of fabricated samples.

Numeric label	Laser scan strategy	Relative Archimedes' density (%)	Areal porosity (%)
1	S0-R90-BF	99.90	0.002
2	S0-R90-UD	100.00	0.003
3	S45-R90-BF	99.95	0.003
4	S45-R90-UD	99.96	0.006
5	S67-R90-BF	99.91	0.002
6	S67-R90-UD	99.92	0.002
7	In-Out	99.91	0.011
8	Out-In	99.86	0.003
9	S0-R120-BF	99.87	0.001
10	S0-R120-UD	99.93	0.098
11	Cage	98.44	0.001
12	Shell	99.93	0.002

strategy was applied on printing cage or shell near the edge respectively, comparable warping deformations were observed to samples fabricated solely using concentric scan strategies (Samples #7 and #8).

3.3. Density and porosity

Density of as-printed parts was measured using Archimedes' methods and subsequently compared to a reference density of 6.481 g/cm^3 (density of bulk material used to prepare the powder) to calculate the relative density. The relative Archimedes' density values of fabricated samples with different laser scan strategies are listed in Table 3. All samples exhibited near-full relative density values (> 99.85 %) except for Sample #11, which was fabricated using cage scan strategy with a distance of 0.5 mm between the outline and the periphery of inner section (Fig. 2). In general, when other process parameters were kept constant (optimized in our previous work [31]), the effect of laser scan strategy on the relative density was negligible due to the comparable energy input. However, it is worth noting that for scan strategies separating the printing area into smaller subsections (e.g., island, stripe), due to the existence of overlap to ensure bonding between subsections, remelting occurred within the overlap regions and increased the overall input energy, which would possibly have a great impact on the density of fabricated sample [32].

Fig. 9 shows the OM images capturing the cross-sections of porosity samples along the building direction. The corresponding areal porosities were determined by image analysis and are listed in Table 3. It can be noticed that except for Sample #10, all samples possessed almost porosity-free cross-sections with areal porosity <0.01 %. Sample #10 exhibited a comparatively high areal porosity (nevertheless still <0.1 %), which is possibly attributed to the fabrication process instability. Even though L-PBF possesses a comparatively high robustness in terms of keeping consistent porosity with identical process parameters, chances still exist when the powder bed flatness, laser status, or the chamber atmosphere slightly changes, and in turn leading to a surge of porosity at certain portions inside the fabricated parts. In addition, it is of high possibility that such high areal porosity found in Sample #10 was not prevalent throughout the fabricated cubic body, in consideration of the high relative Archimedes' density value measured (99.93 %).

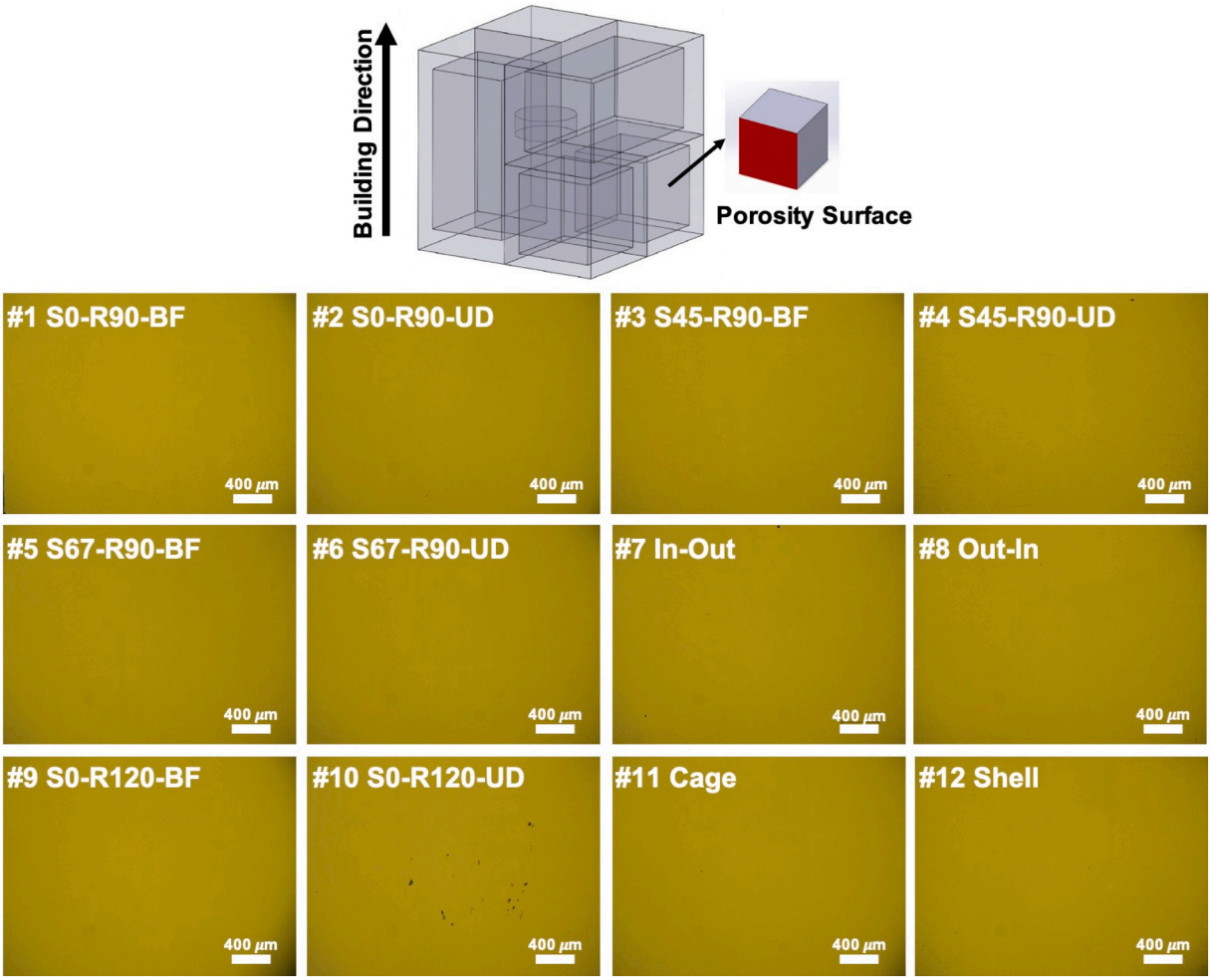

Fig. 9. Cross-sections along the building direction captured under OM of NiTi samples fabricated using different laser scan strategies.

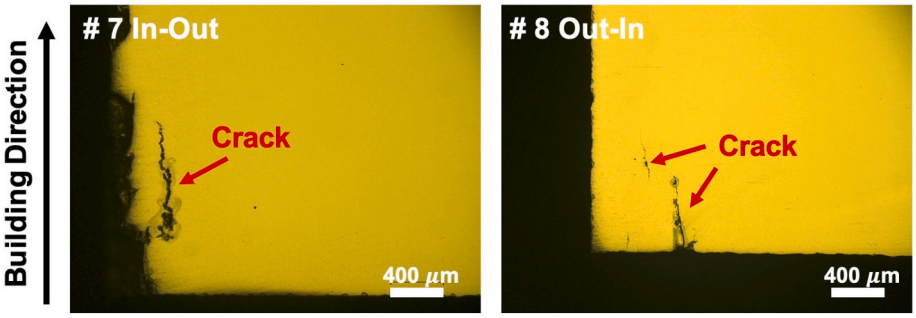

Fig. 10. Cross-sections along the building direction captured under OM of NiTi samples fabricated using In-Out and Out-In laser scan strategies. The arrows indicate the presence of cracks at the bottom.

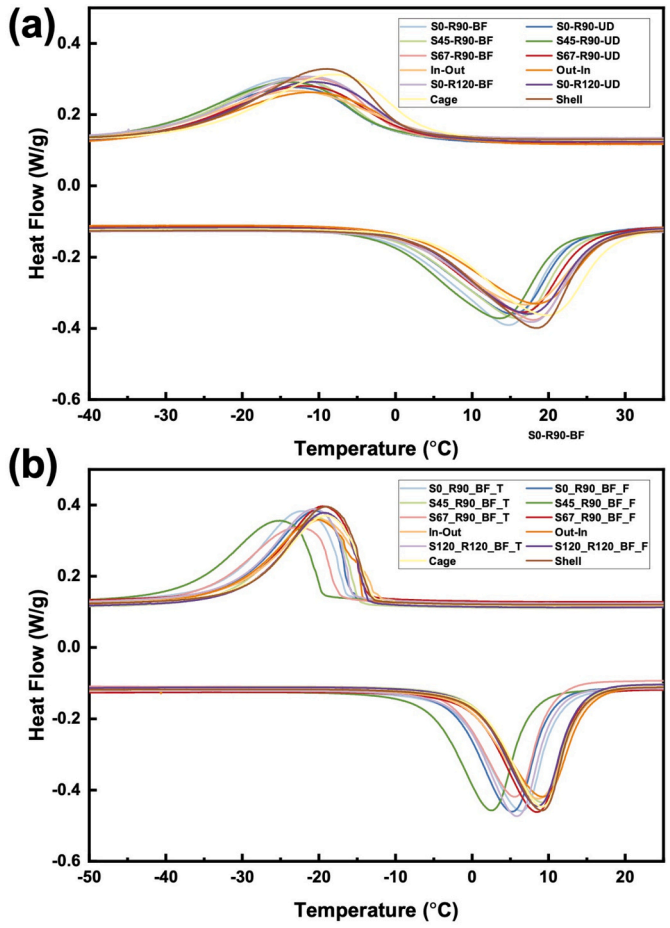

Fig. 11. Phase transformation behavior for the NiTi samples fabricated using different laser scan strategies in (a) as-printed and (b) solution heat treated conditions.

Fig. 10 shows the bottom corner area of the cross-sections fabricated using In-Out and Out-In laser scan strategies. The red arrows indicate the presence of cracks along the building direction. It has been illustrated in Section 3.2 that the samples fabricated by the concentric scan strategies exhibit the largest warping deformation, which is an indication of high residual stress accumulation. Crack formation is another pathway to release high residual stresses. It has been investigated in [42] that the longitudinal residual stress along the building plane was the impetus of the warping distortion and the crack growth, which is in accordance with the results discovered here.

3.4. Phase transformation behavior

To investigate the effect of laser scan strategy on the phase transformation behavior of L-PBF fabricated NiTi parts, DSC results of samples fabricated under different scan strategies in both as-printed and solution heat treated conditions are shown in Fig. 11. After solution heat treatment, the phase transformation peaks become narrower with decreased M_s and A_f temperatures, while M_f and A_s temperatures remain at a comparable level as the as-printed counterparts. Such change in phase transformation behavior can be attributed to the mitigation of the directional residual stress field accumulated during the fabrication process [31]. It is seen that the overall phase transformation behaviors were similar for all samples, mainly due to the same overall input energy during the fabrication process obtained by the identical laser power, scanning speed, and hatch spacing, which resulted in similar amount of Ni differential evaporation. The sample fabricated using S45-R90-UD scan strategy exhibited the lowest transformation temperatures in both as-fabricated and after solution heat treatment conditions. One possible explanation is based on Table 2, this scan strategy has the longest laser jumping time. With the same input energy for different scan strategies, the longer cooling time caused by the longer laser jumping time results in more heat dissipation, which reduces the overall temperature during the manufacturing process and keeps the melt pool at a high temperature for a shorter period of time, ultimately reducing the amount of Ni evaporation and thus the phase transformation temperatures. Details of the transformation temperatures for different laser scan strategies in as-printed and solution heat treated conditions are listed in Table 4 and Table 5 respectively. By using different laser scan strategies, the transformation temperatures (M_s and A_f) and hysteresis variations were kept within 7 °C and 4 °C, respectively. It can be clearly seen that for the concentric scan strategies (In-Out, Out—In), the transformation temperatures are overall higher than the uni-directional or back and forth scan strategies, owing to the fact that the concentric scan strategies possessed less laser jumping time, which resulted in a less amount of time for cooling and heat dissipation during the fabrication process.

3.5. Thermomechanical performance

The thermomechanical performance of NiTi part is closely related to its phase transformation behavior [43]. Owing to parts fabricated using different scan strategies all exhibited similar phase transformation behavior, thermomechanical testing was conducted on one sample to ascertain the fabricated samples possessed acceptable thermomechanical performance. Incremental loading test was conducted on part fabricated by S45-R90-UD scan strategy at the temperature of 35 °C (~ (A_f + 10 °C) for all samples in as-printed condition) and the result is shown in Fig. 12 (a). The incrementally applied strain and recovered strain are illustrated in Fig. 12 (b). The relationships between recovered strain and total applied strain or incrementally applied strain are shown

Table 4
As-printed sample DSC results.

Numeric label	Laser scan strategy	Laser travel time (s)	Ms (°C)	Mf (°C)	As (°C)	Af (°C)	Hysteresis (°C)
1	S0-R90-BF	326	−0.7	−32.1	−1.3	22.5	23.2
2	S0-R90-UD	388	0.9	−34.0	−1.5	23.9	23.0
3	S45-R90-BF	335	−0.1	−32.4	−0.7	24.1	24.2
4	S45-R90-UD	400	−0.2	−33.4	−2.0	22.0	22.2
5	S67-R90-BF	334	1.1	−30.3	1.0	26.0	24.9
6	S67-R90-UD	396	3.2	−31.1	0.0	25.3	22.1
7	In-Out	320	5.8	−34.0	−0.3	27.2	21.4
8	Out-In	320	5.4	−32.6	1.2	28.5	23.1
9	S0-R120-BF	331	2.0	−30.6	1.2	26.2	24.2
10	S0-R120-UD	394	3.3	−30.0	1.1	26.5	23.2
11	Cage	349	5.0	−26.2	4.1	28.8	23.8
12	Shell	346	1.7	−27.3	2.3	26.0	24.3

Table 5
Solution heat treated sample DSC results.

Numeric label	Laser scan strategy	Laser travel time (s)	Ms (°C)	Mf (°C)	As (°C)	Af (°C)	Hysteresis (°C)
1	S0-R90-BF	326	−16.3	−33.1	−2.6	11.1	27.4
2	S0-R90-UD	388	−16.1	−31.6	−2.8	10.2	26.3
3	S45-R90-BF	335	−14.6	−31.2	0.0	13.9	28.5
4	S45-R90-UD	400	−19.5	−37.3	−5.8	7.6	27.1
5	S67-R90-BF	334	−17.5	−35.3	−2.8	10.4	27.9
6	S67-R90-UD	396	−13.7	−30.1	−0.2	13.5	27.2
7	In-Out	320	−12.9	−31.5	−1.1	14.7	27.6
8	Out-In	320	−14.3	−32.0	−0.5	15.2	29.5
9	S0-R120-BF	331	−15.7	−31.6	−2.2	10.8	26.5
10	S0-R120-UD	394	−14.4	−30.1	−0.1	13.8	28.2
11	Cage	349	−13.1	−29.7	0.5	14.0	27.1
12	Shell	346	−13.1	−29.2	0.4	13.8	26.9

in Fig. 12 (c) and (d) respectively. Similar to what has been reported in [31], perfect superelasticity was not achieved (i.e., recovered strain = total applied strain). After the first loading cycle, the superelasticity of as-printed part degraded rapidly.

In general, for Ni-rich NiTi components, superelasticity is achieved by homogeneous Ni_4Ti_3 nanoprecipitation [44]. In this study, the degradation of superelasticity is possibly due to lack of Ni_4Ti_3 precipitates generation. During L-PBF process, the differential evaporation of Ni resulted in a lower Ni/Ti ratio in the printed part compared to the starting powder. As a result, no sufficient amount of Ni was available to form Ni_4Ti_3 precipitates. By comparing the incremental loading test results in this study with [31], in which a different laser scan strategy (S45-R90-BF) was used keeping other process parameters identical, it is validated that the effect of scan strategy on the superelasticity of L-PBF fabricated NiTi structures is negligible.

The stress-strain curves representing the shape recovery behavior of the compression sample fabricated using the laser scan strategy S0-R90-BF are shown in Fig. 13 (a). The sample was compressed to the strain magnitudes of 2 % (red lines) and 4 % (blue lines) at −50 °C (in martensite phase) and unloaded to zero stress, and then subsequently heated up to 100 °C (in austenite phase) in order to measure the recovery ratio and quantify the shape memory property. The recoverable strains are shown as dashed arrows in Fig. 13 (a), and a summary of the recovered strains at different applied strain levels are shown in Fig. 13 (b). It could be clearly noticed that recovery strain of up to 3 % was obtained after compressive deformation of 4 %. As compared to the result reported in [31], in which scan strategy S45-R90-BF was applied, similar shape recovery behavior was obtained, indicating that the shape memory effect is insensitive to the applied laser scan strategy.

4. Conclusions

In the present study, the effect of laser scan strategy on the fabrication outcome of Ni-rich $Ni_{50.8}Ti_{49.2}$ (at. %) shape memory alloys (SMAs) by laser powder bed fusion (L-PBF) process was investigated. Fabrication time, warping deformation, top surface morphology, density/porosity, phase transformation behavior, shape memory and superelastic properties were compared among samples fabricated by 12 distinct laser scan strategies. With all other process parameters (e.g. laser power, scanning speed, hatch spacing, layer thickness) kept constant, the effect of individual change of laser scan strategy on different properties of the fabricated part was evident. The current study serves as a guideline to select adequate laser scan strategies for manufacturing NiTi SMAs via L-PBF. No scan strategy excelled in all evaluation metrics simultaneously, indicating that the scan strategy must be selected based on desired final properties and manufacturing constraints. Main conclusions can be summarized as follows:

1. Laser scan strategy exerted significant effects on the level of warping deformation. Concentric scan strategies resulted in more severe warping deformation compared to uni-directional or back and forth strategies, which was attributed to the long scanning vectors and accumulated residual stress build-up along specific directions.
2. Uni-directional or back and forth scan strategies with an angle to the edge of the part exhibited material accumulation at the corners and resulted in the elevated corner phenomenon. Single-directional scan strategy alleviated such phenomenon to a certain extent compared to the back and forth counterparts. Shell scan strategy also relieved such phenomenon.
3. The samples fabricated using different scan strategies all obtained near full densities with porosity <0.1 % with careful selection of other key process parameters of laser power, scanning speed, hatch spacing, and layer thickness.
4. The phase transformation behavior and resulting thermomechanical properties were similar for all samples in both as-fabricated and solution heat treated conditions, mainly due to similarity in the overall input energy during fabrication process, which resulted in comparable amounts of Ni differential evaporation. The difference in cooling time showed minor effect on the variation of transformation temperatures.

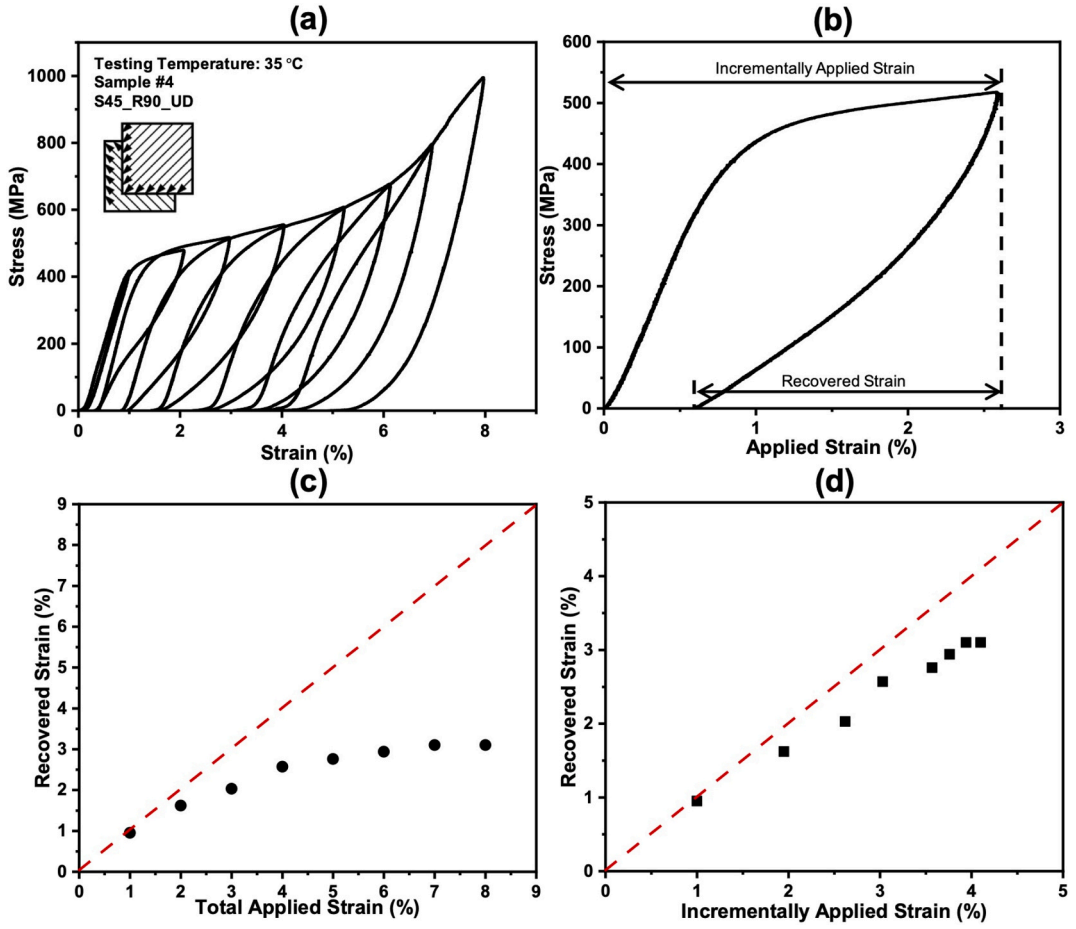

Fig. 12. (a) The results of incremental loading test performed at 35 °C on the compression sample fabricated using the scan strategy of S45-R90-UD. (b) Illustration of incrementally applied strain and recoverable strain of the cycle with the total applied strain of 3 %. (c) The relationship between total applied strain and recovered strain. (d) The relationship between incrementally applied strain and recovered strain.

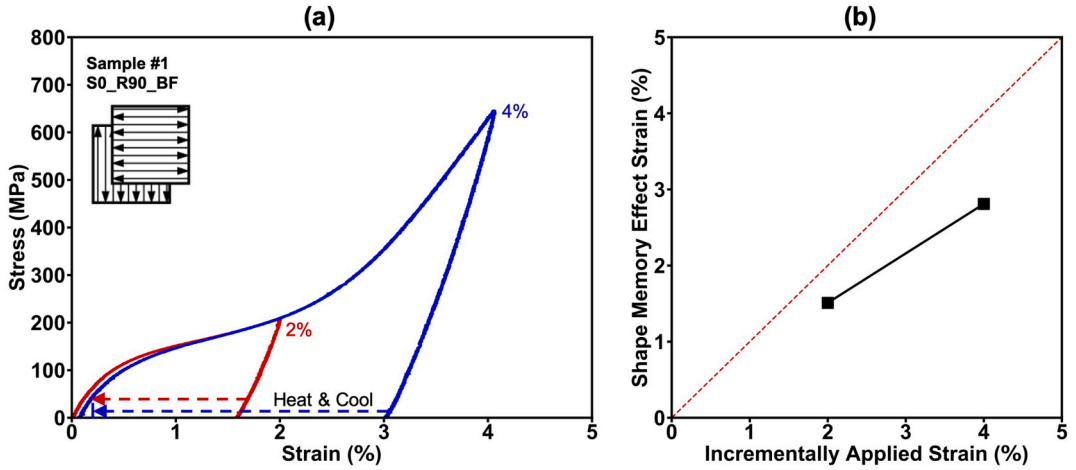

Fig. 13. (a) Stress-strain curves showing the shape recovery behavior of the compression sample fabricated using the laser scan strategy S0-R90-BF. The sample was compressed to the strain magnitudes of 2 % (red lines) and 4 % (blue lines) at −50 °C in martensite and unloaded to zero stress, followed by heating up to 100 °C in austenite to recover the deformation (dashed arrows). (b) The recoverable strain vs. the applied strain at the strain magnitudes of 2 % and 4 %. (For interpretation of the references to color in this figure legend, the reader is referred to the web version of this article.)

5. Since the total fabrication time for different laser scan strategies was different while increasing the manufacturing time will increase the energy consumption, under the circumstance where the acceptable part properties could be achieved via more than one laser scan strategies, the strategy with minimum energy consumption (minimum fabricating time) should be utilized.

Declaration of competing interest

The authors declare that they have no known competing financial interests or personal relationships that could have appeared to influence the work reported in this paper.

Acknowledgments

The co-authors thank the support from National Science Foundation (NSF) through Grant No. 1846676. AE, IK, and RA also would like to thank funding support from Schlumberger.

References

[1] Buehler WJ, Gilfrich J, Wiley R. Effect of low-temperature phase changes on the mechanical properties of alloys near composition tini. J Appl Phys 1963;34(5):1475–7.
[2] Wang FE, Buehler WJ, Pickart SJ. Crystal structure and a unique “martensitic” transition of tini. J Appl Phys 1965;36(10):3232–9.
[3] Otsuka K, Wayman CM. Shape memory materials. Cambridge University Press; 1999.
[4] Shabalovskaya SA. On the nature of the biocompatibility and on medical applications of niti shape memory and superelastic alloys. Biomed Mater Eng 1996;6(4):267–89.
[5] Es-Souni M, Es-Souni M, Fischer-Brandies H. Assessing the biocompatibility of niti shape memory alloys used for medical applications. Anal Bioanal Chem 2005;381(3):557–67.
[6] Hartl DJ, Lagoudas DC. Aerospace applications of shape memory alloys. Proc. Inst. Mech. Eng. G 2007;221(4):535–52.
[7] Jani JM, Leary M, Subic A, Gibson MA. A review of shape memory alloy research, applications and opportunities. Mater Des 2014;1980–2015(56):1078–113.
[8] Elahinia M, Moghaddam NS, Andani MT, Amerinatanzi A, Bimber BA, Hamilton RF. Fabrication of NiTi through additive manufacturing: a review. Prog Mater Sci 2016;83:630–63.
[9] Mahmoudi M, Tapia G, Franco B, Ma J, Arroyave R, Karaman I, Elwany A. On the printability and transformation behavior of nickel-titanium shape memory alloys fabricated using laser powder-bed fusion additive manufacturing. JManuf Process 2018;35:672–80.
[10] Dadbakhsh S, Speirs M, Kruth J-P, Van Humbeeck J. Influence of slm on shape memory and compression behaviour of niti scaffolds. CIRP Ann 2015;64(1):209–12.
[11] Dadbakhsh S, Speirs M, Kruth J-P, Schrooten J, Luyten J, Van Humbeeck J. Effect of slm parameters on transformation temperatures of shape memory nickel titanium parts. Adv Eng Mater 2014;16(9):1140–6.
[12] Yang Y, Zhan J, Sun Z, Wang H, Lin J, Liu Y, Zhang L. Evolution of functional properties realized by increasing laser scanning speed for the selective laser melting fabricated NiTi alloy. J Alloys Compd 2019;804:220–9.
[13] Shishkovsky I, Yadroitsev I, Smurov I. Direct selective laser melting of nitinol powder. Phys Procedia 2012;39:447–54.
[14] Jia Q, Gu D. Selective laser melting additive manufacturing of inconel 718 superalloy parts: densification, microstructure and properties. J Alloys Compd 2014;585:713–21.
[15] Thijs L, Verhaeghe F, Craeghs T, Van Humbeeck J, Kruth J-P. A study of the microstructural evolution during selective laser melting of Ti–6Al–4V. Acta Mater 2010;58(9):3303–12.
[16] Saedi S, Moghaddam NS, Amerinatanzi A, Elahinia M, Karaca HE. On the effects of selective laser melting process parameters on microstructure and thermomechanical response of Ni-rich niti. Acta Mater 2018;144:552–60.
[17] Haberland C, Elahinia M, Walker JM, Meier H, Frenzel J. On the development of high quality niti shape memory and pseudoelastic parts by additive manufacturing. Smart Mater Struct 2014;23(10):104002.
[18] Bormann T, Schumacher R, Mertmann M, M¨uller B, de Wild M. Tailoring selective laser melting process parameters for niti implants. Journal of Materials Engineering and Performance 2012;21(12):2519–24.
[19] Speirs M, Wang X, Van Baelen S, Ahadi A, Dadbakhsh S, Kruth J-P, Van Humbeeck J. On the transformation behavior of niti shape-memory alloy produced by slm. Shape Mem Superelast 2016;2(4):310–6.
[20] Marattukalam JJ, Singh AK, Datta S, Das M, Balla VK, Bontha S, Kalpathy SK. Microstructure and corrosion behavior of laser processed niti alloy. Mater Sci Eng C 2015;57:309–13.
[21] Ou S-F, Peng B-Y, Chen Y-C, Tsai M-H. Manufacturing and characterization of niti alloy with functional properties by selective laser melting. Metals 2018;8(5):342.
[22] Yang Y, Zhan J, Li B, Lin J, Gao J, Zhang Z, Ren L, Castany P, Gloriant T. Laser beam energy dependence of martensitic transformation in slm fabricated niti shape memory alloy. Materialia 2019;6:100305.
[23] Gouveia RM, Silva FJ, Atzeni E, Sormaz D, Alves JL, Pereira AB. Effect of scan strategies and use of support structures on surface quality and hardness of l-pbf alsi10mg parts. Materials 2020;13(10):2248.
[24] Rashid R, Masood S, Ruan D, Palanisamy S, Rashid RR, Elambasseril J, Brandt M. Effect of energy per layer on the anisotropy of selective laser melted alsi12 aluminium alloy. Addit Manuf 2018;22:426–39.
[25] Zhang H, Peng T, Xu S. The influence of scanning pattern on the part properties in powder bed fusion processes: an experimental study. Procedia CIRP 2017;61:606–11.
[26] Arısoy YM, Criales LE, Ozel T, Lane B, Moylan S, Donmez A. Influence of scan strategy and process parameters on microstructure and its optimization in additively manufactured nickel alloy 625 via laser powder bed fusion. International Journal of Advanced Manufacturing Technology 2017;90(5):1393–417.
[27] Kudzal A, McWilliams B, Hofmeister C, Kellogg F, Yu J, Taggart-Scarff J, Liang J. Effect of scan pattern on the microstructure and mechanical properties of powder bed fusion additive manufactured 17–4 stainless steel. Mater Des 2017;133:205–15.
[28] Ramos D, Belblidia F, Sienz J. New scanning strategy to reduce warpage in additive manufacturing. Addit Manuf 2019;28:554–64.
[29] Song J, Wu W, Zhang L, He B, Lu L, Ni X, Long Q, Zhu G. Role of scanning strategy on residual stress distribution in Ti-6Al-4V alloy prepared by selective laser melting. Optik 2018;170:342–52.
[30] Cheng B, Shrestha S, Chou K. Stress and deformation evaluations of scanning strategy effect in selective laser melting. Addit Manuf 2016;12:240–51.
[31] Xue L, Atli K, Picak S, Zhang C, Zhang B, Elwany A, Arroyave R, Karaman I. Controlling martensitic transformation characteristics in defect-free niti shape memory alloys fabricated using laser powder bed fusion and a process optimization framework. Acta Mater 2021;215:117017.
[32] Guo W, Sun Z, Yang Y, Wang X, Xiong Z, Li Z, Wang C, Cui L, Huang S, Li M, et al. Study on the junction zone of niti shape memory alloy produced by selective laser melting via a stripe scanning strategy. Intermetallics 2020;126:106947.
[33] Lu Y, Wu S, Gan Y, Huang T, Yang C, Junjie L, Lin J. Study on the microstructure, mechanical property and residual stress of slm inconel-718 alloy manufactured by differing island scanning strategy. Optics Laser Technol 2015;75:197–206.
[34] Matache G, Vladut M, Paraschiv A, Condruz RM. Edge and corner effects in selective laser melting of in 625 alloy. Manuf Rev 2020;7:8.
[35] Zhang C, Xue L, Atli KC, Arroyave R, Karaman I, Elwany A. On the fabrication of defect-free nickel-rich nickel-titanium parts using laser powder bed fusion. J Manuf Sci Eng 2022:1–31.
[36] Khoo ZX, Liu Y, An J, Chua CK, Shen YF, Kuo CN. A review of selective laser melted niti shape memory alloy. Materials 2018;11(4):519.
[37] Xue L, Atli K, Zhang C, Hite N, Srivastava A, Leff A, Wilson A, Sharar D, Elwany A, Arroyave R, et al. Laser powder bed fusion of defect-free niti shape memory alloy parts with superior tensile superelasticity. Acta Mater 2022;229:117781.
[38] Parry L, Ashcroft I, Wildman RD. Understanding the effect of laser scan strategy on residual stress in selective laser melting through thermo-mechanical simulation. Addit Manuf 2016;12:1–15.
[39] Oliveira JP, LaLonde A, Ma J. Processing parameters in laser powder bed fusion metal additive manufacturing. Mater Des 2020;193:108762.
[40] Promoppatum P, Yao S-C. Influence of scanning length and energy input on residual stress reduction in metal additive manufacturing: numerical and experimental studies. J Manuf Process 2020;49:247–59.
[41] Waqar S, Guo K, Sun J. Fem analysis of thermal and residual stress profile in selective laser melting of 316l stainless steel. J Manuf Process 2021;66:81–100.
[42] Mukherjee T, Zhang W, DebRoy T. An improved prediction of residual stresses and distortion in additive manufacturing. Comput Mater Sci 2017;126:360–72.
[43] Frenzel J, George EP, Dlouhy A, Somsen C, Wagner M-X, Eggeler G. Influence of Ni on martensitic phase transformations in niti shape memory alloys. Acta Mater 2010;58(9):3444–58.
[44] Elahinia MH, Hashemi M, Tabesh M, Bhaduri SB. Manufacturing and processing of niti implants: a review. Prog Mater Sci 2012;57(5):911–46.